Article

The key role of forest disturbance in reconciling estimates of the northern carbon sink

Check for updates

Michael O'Sullivan [1] ✉, Stephen Sitch [1], Pierre Friedlingstein [1,2], Ingrid T. Luijkx [3], Wouter Peters [3], Thais M. Rosan [1], Almut Arneth[4], Vivek K. Arora[5], Naveen Chandra [6], Frédéric Chevallier [7], Philippe Ciais[7], Stefanie Falk [8], Liang Feng[9,10], Thomas Gasser [11], Richard A. Houghton[12], Atul K. Jain [13], Etsushi Kato [14], Daniel Kennedy[15], Jürgen Knauer [16,17], Matthew J. McGrath[7], Yosuke Niwa [18,19], Paul I. Palmer [9,10], Prabir K. Patra [6,20], Julia Pongratz[8,21], Benjamin Poulter [22], Christian Rödenbeck [23], Clemens Schwingshackl [8], Qing Sun [24,25], Hanqin Tian [26], Anthony P. Walker [27], Dongxu Yang[28], Wenping Yuan [29], Xu Yue [30] & Sönke Zaehle [23]

Northern forests are an important carbon sink, but our understanding of the driving factors is limited due to discrepancies between dynamic global vegetation models (DGVMs) and atmospheric inversions. We show that DGVMs simulate a 50% lower sink (1.1 ± 0.5 PgC yr^{-1} over 2001–2021) across North America, Europe, Russia, and China compared to atmospheric inversions (2.2 ± 0.6 PgC yr^{-1}). We explain why DGVMs underestimate the carbon sink by considering how they represent disturbance processes, specifically the overestimation of fire emissions, and the lack of robust forest demography resulting in lower forest regrowth rates than observed. We reconcile net sink estimates by using alternative disturbance-related fluxes. We estimate carbon uptake through forest regrowth by combining satellite-derived forest age and biomass maps. We calculate a regrowth flux of 1.1 ± 0.1 PgC yr^{-1}, and combine this with satellite-derived estimates of fire emissions (0.4 ± 0.1 PgC yr^{-1}), land-use change emissions from bookkeeping models (0.9 ± 0.2 PgC yr^{-1}), and the DGVM-estimated sink from CO_2 fertilisation, nitrogen deposition, and climate change (2.2 ± 0.9 PgC yr^{-1}). The resulting 'bottom-up' net flux of 2.1 ± 0.9 PgC yr^{-1} agrees with atmospheric inversions. The reconciliation holds at regional scales, increasing confidence in our results.

Terrestrial ecosystems currently play a significant role in mitigating climate change by acting as a net carbon sink, absorbing between 1.1 and 1.6 PgC yr^{-1} (2001–2021 average; as estimated by process-models and atmospheric constraints)[1]. To develop robust projections that describe how the land carbon sink will respond to future environmental change, we need a comprehensive understanding of the drivers and processes, and identification of the regions responsible for contemporary carbon sinks.

Observed large-scale gradients in atmospheric CO_2 indicate that northern ecosystems contribute more to the global net land carbon sink mean and trend than tropical lands[2]. The global network of observations can be used to constrain atmospheric inversion systems. Inversion systems combine these CO_2 measurements with atmospheric transport model output to produce gridded estimates of net land-atmosphere carbon exchange. In general, due to sparse atmospheric monitoring networks, as well as inherent uncertainties in inversion modelling, confidence in fluxes starts at aggregates across large ecosystems, and increases to continental and semi-hemispheric scales[3,4].

Process-based models, known as dynamic global vegetation models (DGVMs), also suggest an increasing northern carbon sink. DGVMs attribute this trend to long-term warming[5,6] and to increased atmospheric CO_2 concentrations and nitrogen deposition[7,8], which can increase photosynthesis and biomass production[9,10]. Further, expanding forest area is also a key driver of increased carbon uptake[11]. Overall, DGVMs predict CO_2 fertilisation to be the main driver of the northern carbon sink[12–14]. However, DGVMs simulate a 50% lower land carbon sink (1.1 ± 0.5 PgC yr^{-1}) in northern lands (defined in this study as North America, Europe, Russia, and

China) compared to atmospheric inversions (2.2 ± 0.6 PgC yr^{-1}), over 2001–2021 (Fig. 1a).

A significant proportion of northern forests are regrowing due to historical land-use changes, variations in harvesting intensity and other forest management practices, or due to recovery from natural disturbances. These factors are estimated to contribute up to 1.3 PgC yr^{-1} to the observed northern carbon sink[11,15,16], and DGVMs potentially underestimate this sink. Many DGVMs have insufficient representations of disturbance processes, in particular simulating carbon losses from wildfire, windthrow or pests[17]. Likewise, land-cover change and land management (in forests and agricultural lands) are also implemented imperfectly[16,18]. Further, the subsequent regrowth from disturbance events tends to be underestimated by some models, leading to lower than expected carbon uptake. In reality, the area affected by a natural disturbance could initially become a strong carbon source and later a strong sink during its recovery phase[19–21]. These shortcomings are partly attributable to most DGVMs missing the role of forest age structure on disturbance and biomass production[15].

The challenges are not only incomplete process-representations in DGVMs. Two DGVMs here (CABLE-POP and LPJ-GUESS) do simulate forest demography, but there is a lack of robust historical information about natural disturbance and land use and land management, which would enable these models to achieve better estimates[22,23]. For example, DGVMs do not capture the intense forest management in the early modern period and thus may underestimate regrowth[24]. Currently, a large-scale observational dataset of the northern carbon sink from forest regrowth does not exist for the period 2001–2021. We therefore pose the questions:

Can we reconcile the inversion and DGVM northern sink estimates with the inclusion of observationally constrained estimates of disturbance carbon losses (from fire and land-use change), and subsequent forest regrowth?

What is the contribution of (1) indirect carbon sink due to rising atmospheric CO_2 concentrations, nitrogen deposition, and climate change, (2) land-use and land-cover change carbon losses, (3) wildfire carbon losses, and (4) age-related regrowth, to the northern carbon sink?

In this study, we develop a satellite-based estimate of the forest regrowth flux by studying region-specific age-biomass relationships (derived from *MPI-BGC forest age*[25], and *ESA-CCIv4 biomass*[26] maps which are representative of the year 2010; see 'Methods'). Regrowth fluxes are estimated at 1 km resolution for each year over 2001–2021, explicitly accounting for the impact of fire disturbance on regrowth using satellite-derived burned areas for years post-2010[27]. We combine this new forest regrowth estimate with satellite-derived wildfire emission data[28] and carbon losses from three bookkeeping models[1] to explain the northern carbon sink difference between DGVMs and atmospheric inversions. We focus on four regions: North America (USA and Canada), Europe, Russia, and China. These regions are selected as they are the countries with major transitions from agriculture to secondary forest in recent decades[29].

Results and discussion
Forest age and wildfire are poorly represented in DGVMs
For the four study regions combined, the DGVMs simulate a net carbon sink of 1.1 ± 0.5 PgC yr^{-1}, much lower than the atmospheric inversion estimate of 2.2 ± 0.6 PgC yr^{-1}, over the years 2001–2021 (Fig. 1a). We suggest two of the contributing factors to this mismatch are overestimations of simulated wildfire emissions in DGVMs, and an underestimation of carbon uptake in the regrowing forests of the northern hemisphere. CABLE-
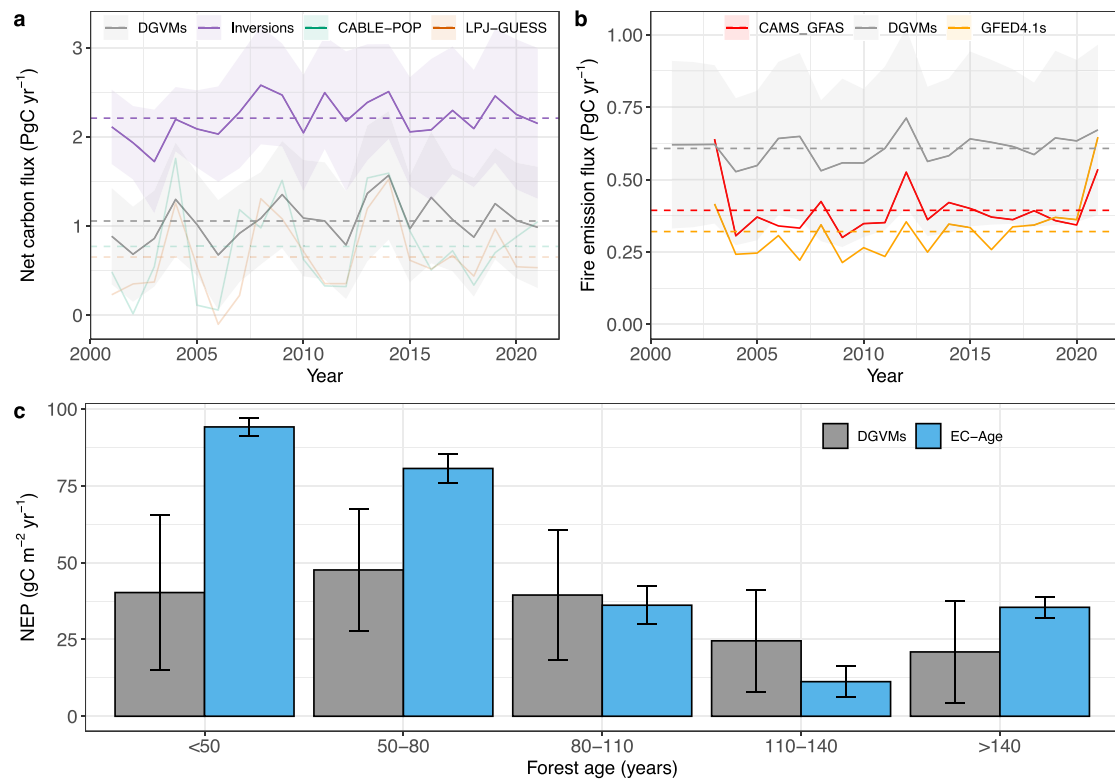

Fig. 1 | Large discrepancy in northern carbon sink between bottom-up and top-down estimates can be explained by disturbance processes. a Mean net carbon flux for North America, Europe, Russia, and China combined for dynamic global vegetation models (DGVMs) (grey), atmospheric inversions (purple), and the two demography-enabled DGVMs; CABLE-POP (green) and LPJ-GUESS (orange). Positive values are a net uptake by land. Dashed lines show mean values over the study period and shading represents 1σ model spread. b Wildfire carbon emissions for the four regions as estimated by the DGVMs (grey), and by two remote-sensing products; GFAS (red) and GFED4.1 s (orange). c Net ecosystem production (NEP) estimates from DGVMs (grey) and upscaled eddy covariance data (EC-Age), which has been adjusted for tree age (blue). The NEP fluxes are partitioned into forest age classes. Here we show gridbox mean NEP for the DGVMs, which includes non-forest fluxes. However, in general, forest NEP has a dominant control on gridbox NEP in the regions considered in this study (Supplementary Fig. 1).
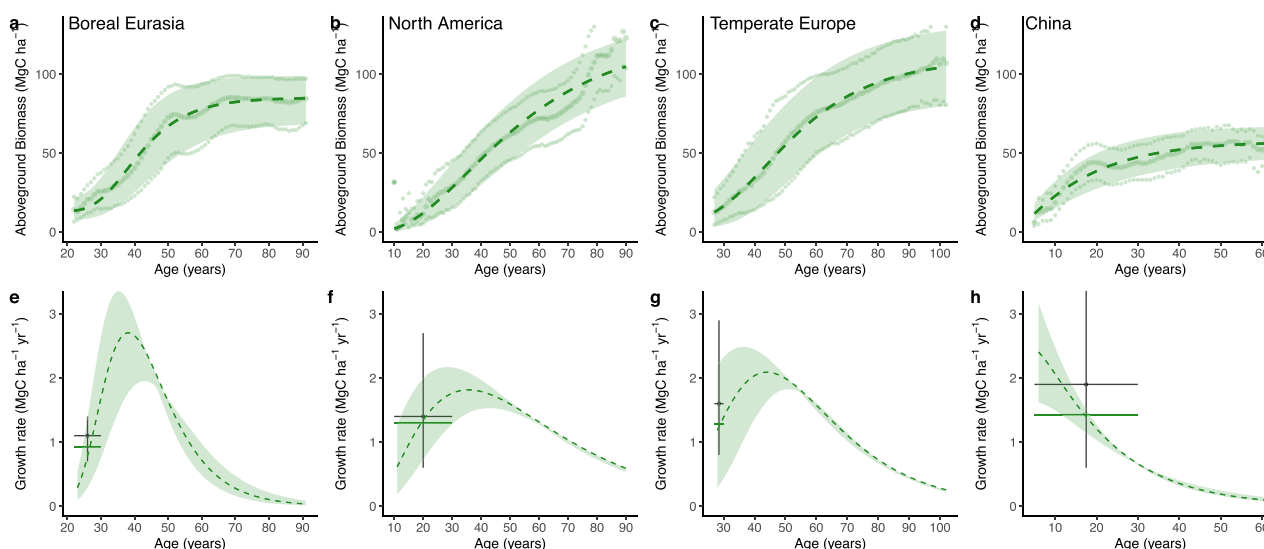
Fig. 2 | Satellite-derived regrowth curves for northern forests. a–d Panels show the effect of forest age (years) on aboveground biomass (MgC ha^{-1} yr^{-1}) in a subset of the four regions; **a** Boreal Eurasia, **b** North America, **c** Temperate Europe, and **d** China. Points indicate the 25th, 50th, and 75th percentile of satellite-based biomass values across all pixels for each year. Best fit lines (dashed and shading) are shown and are used to calculate annual growth increment. **e–h** Panels depict the annual growth increment for the four regions. Dashed lines and shading represent the 25th, 50th, and 75th percentile estimates. The solid green horizontal line is the mean growth for the first 30 years. The black point and range show in situ observations (ref. 37) of growth rates for trees younger than 30 years. Note, we have truncated the y-axis in (**h**), the upper limit for in situ growth rates in China is 4.9 MgC ha^{-1} yr^{-1}.

POP and LPJ-GUESS (both include explicit forest demography) simulate a net land carbon sink below the DGVM mean (Fig. 1a). This indicates it is not sufficient for DGVMs to only include demographic processes, but to also be constrained with detailed information on historical disturbance and land management[24,29].

DGVMs estimate northern fire carbon emissions of 0.6 ± 0.3 PgC yr^{-1} over 2003–2021, whereas satellite-derived estimates suggest lower emissions of 0.3 and 0.4 PgC yr^{-1} (GFED and GFAS, respectively) (Fig. 1b). This overestimation is likely driven by issues with modelled burned areas (ignition and fire spread parameterisations and sensitivity to environmental conditions[17]) and combustion completeness in DGVMs[30]. There is also a lack of available information on fire control measures that some countries implement, which does not allow DGVMs to include these in their fire algorithms. Both 2003 and 2021 experienced anomalously high fire emissions, predominantly driven by warm conditions in Russia[31,32], however, notably, the DGVMs do not simulate a large deviation from mean emissions (Fig. 1).

Next, using a forest age map[25], we aggregate the mean net ecosystem production (NEP, defined as the net flux of carbon into the land in the absence of disturbances) flux for the DGVMs into various age classes and compare with upscaled forest NEP derived from eddy-covariance data, along with climate variables and forest age (EC-Age) (see 'Methods') (Fig. 1c). Many DGVMs do not output forest NEP, as they use a single soil column for all vegetation. However, in general, forest NEP is highly correlated with gridbox NEP in the regions considered here (Supplementary Fig. 1). Therefore, we use grid-box NEP as a proxy for forest NEP in the comparison with EC-Age. There is a clear pattern of DGVMs, on average, underestimating the carbon uptake in lands containing young forests. DGVMs simulate net rate of carbon uptake of 40 ± 25 gC m^{-2} yr^{-1} compared with 98 ± 3 gC m^{-2} yr^{-1} for EC-Age in forests younger than 50 years old, and 48 ± 20 gC m^{-2} yr^{-1} compared with 80 ± 4 gC m^{-2} yr^{-1} for forests 50–80 years old. The two estimates have good agreement in regions of older-growth (>80 years) forests (Fig. 1c).

The relatively uniform distribution of carbon uptake across age classes is expected for the DGVMs that do not represent demography. These models simulate average plants, rather than multiple age cohorts, with different growth rates. Therefore, when a forest is disturbed, a portion of

biomass is removed from the grid average forest. This generally reduces the average forest biomass slightly below its equilibrium old-growth value, and therefore the subsequent regrowth is relatively slow. If an entire gridcell was deforested, one could expect the DGVMs to capture the correct regrowth rates. Therefore, it may not be regrowth rates, per se, that are wrong in DGVMs, but that they are not able to simulate disturbance in ecosystems correctly, due to simulating average plants, running at coarse spatial resolution, and not accurately simulating the actual year of natural disturbance.

The DGVMs do suggest a minor decline in net carbon uptake over time, which could be driven by increased respiratory costs of larger trees[33], or self-thinning and canopy packing constraints[34] leading to increased losses for the models that include this stand-level process. An alternative explanation is that many old-growth forests are concentrated in regions with worsening climate conditions (e.g. drought-prone areas of the North American west coast and fire-prone regions in Eastern Siberia[35]), which could result in reduced carbon uptake in DGVMs[36].

Forest age limits carbon accumulation over large regions

A space-for-time analysis (see 'Methods') comparing forest age and biomass maps (both for 2010), shows clear regrowth patterns, with biomass increasing with age, and levelling off after several decades (Fig. 2a–d). Temperate forests of North America and Europe approach aboveground carbon densities of 123 [104,138] MgC ha^{-1} and 107 [80,130] MgC ha^{-1} (maximum 50th [25th, 75th] biomass percentiles across all years), whereas the boreal forests of Eurasia peak lower at 85 [69,97] MgC ha^{-1} (Fig. 2). Forests in China have relatively low aboveground carbon densities of 58 [48,64] MgC ha^{-1}. These maximum values are consistent with a recent meta-analysis of forest plot carbon accumulation, whereby boreal forests peak below 100 MgC ha^{-1}, and temperate species can reach carbon densities >100 MgC ha^{-1} after 100 years of growth[37].

We fit region-specific regrowth curves (Chapman-Richards model[38]) to estimate changes in biomass over time. The derivative of biomass vs. age curves gives us the biomass carbon sink from forest growth at a given age. Peak growth (maximum derivative) occurs before trees are 50 years old in all regions, and there is an abundance of these young trees across northern lands (Supplementary Fig. 2). For North America, temperate Europe, and Eurasia, growth rates peak at approximately 2 MgC ha^{-1} yr^{-1} when trees are
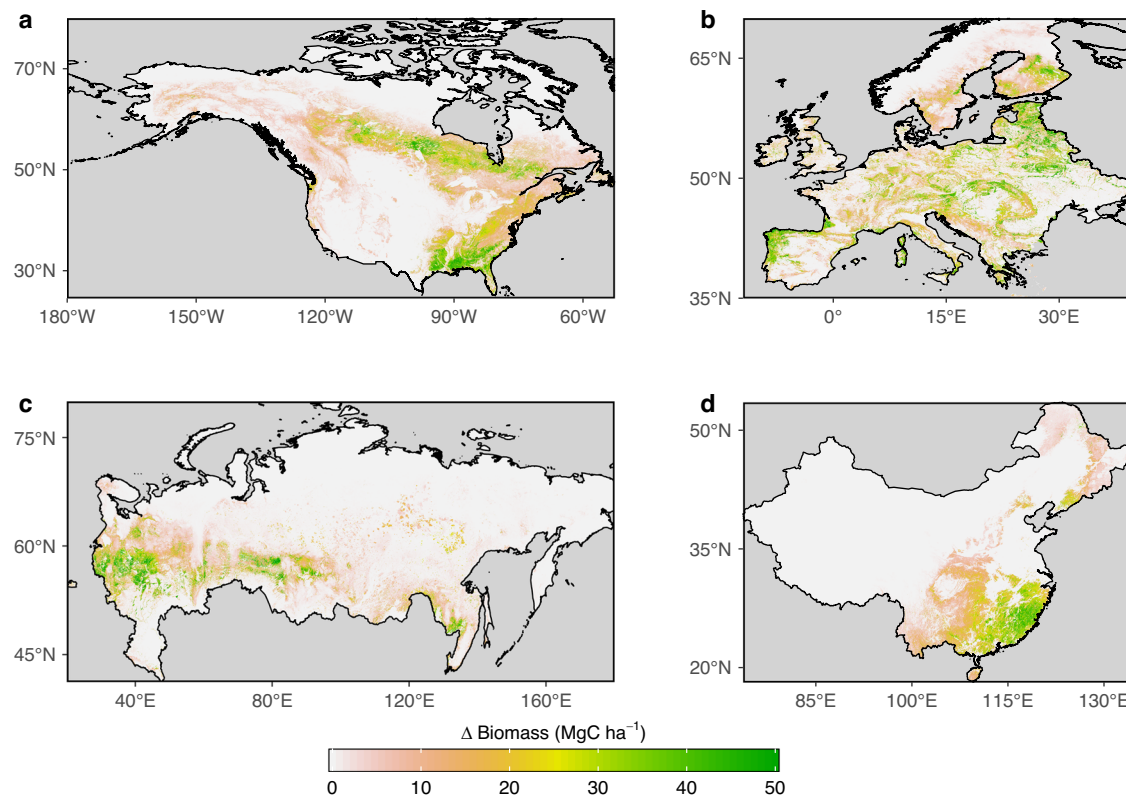
Fig. 3 | Substantial regional carbon uptake due to forest regrowth over the last two decades. Maps depict the cumulative carbon sink due to forest regrowth over 2001–2021 based on satellite-derived regrowth curves (MgC ha^{-1}). For each pixel, the growth depends on regional growth curves (Fig. 2) and the inferred forest age[25] starting in 2001. Each year, the forest age increases and a new growth value is calculated. In the years 2010–2021, the age of a pixel is set to 1 if disturbance is detected. Non-forest pixels are removed from the analysis.

~40 years old. For China, peak growth occurs earlier, when trees are younger than 20 years. Average growth rates for trees younger than 30 years agree well with in situ observations across all regions (Fig. 2[37]). We combine these growth rates with the forest age map to predict regrowth carbon uptake for each 1 km pixel for each year 2001–2021. The largest cumulative changes in biomass due to forest regrowth are located along the east coast of the USA, central Canada, western Russia, central/northern Europe, and southeast China (Fig. 3). Across central and eastern Russia, there are many localised regions of regrowth following fire disturbance. Wildfire-induced losses and recovery have previously been shown to strongly influence carbon cycle dynamics in this region[35].

Reconciling the northern carbon sink and attribution of drivers

We reconcile the atmospheric inversion and DGVM estimates of net carbon uptake across the four study regions by combining DGVM net ecosystem production with independent estimates of disturbance-related carbon fluxes (Fig. 4). First, DGVM NEP (from the simulation without land-use and land-cover change (S2; see 'Methods') and only fire-enabled DGVMs) is estimated to be 2.2 ± 0.9 PgC yr^{-1}, and is primarily driven by rising CO_2 concentrations and nitrogen deposition[12], and regional impacts of climate change (warming and subsequent lengthening of the growing season[39,40]). Second, emissions such as from deforestation by clearing or fire or decay of wood products, as well as peat drainage are 0.9 ± 0.2 PgC yr^{-1} across the four regions. The majority of these emissions occur from wood harvest (gross losses of 0.5 ± 0.2 PgC yr^{-1}), and the remainder from deforestation and other land-use changes (0.2 ± 0.03 PgC yr^{-1}), and peat drainage (0.1 ± 0.02 PgC yr^{-1}). Wood harvest forcing data is taken from FAO, and associated carbon losses are a relatively well-constrained component of the net carbon balance. Third, fire emissions amount to 0.4 ± 0.1 PgC yr^{-1}. Fourth, In response to past disturbances, forest regrowth across northern lands

sequesters 1.1 ± 0.1 PgC yr^{-1}, over 2001–2021. The sum of the four component fluxes (DGVM NEP, bookkeeping LULCC, satellite fire losses, and satellite regrowth) indicates a net carbon sink of 2.0 ± 0.9 PgC yr^{-1}, in-line with the top-down constraint of 2.2 ± 0.6 PgC yr^{-1}.

Using only non-fire DGVMs, the NEP is 1.1 ± 0.2 PgC yr^{-1} and the sum of component fluxes is only 1.0 ± 0.3 PgC yr^{-1}, and therefore these models cannot be reconciled with atmospheric inversions (Fig. 4a, black crosses). The number of disturbance processes and their particular formulation included in DGVMs has a major impact on NEP. This is simply because carbon is released to the atmosphere via fire or land management before being respired naturally, as part of the heterotrophic respiration flux. Further, subsequent regrowth following disturbance can enhance NEP. Therefore, in models with more disturbance processes included, the NEP values are generally larger. We argue that models that do not include any major disturbance processes likely underestimate NEP, as they are closer to equilibrium than reality (Fig. 4a). In other words, by using non-fire models in conjunction with the satellite-based fire emission products, we double count some carbon losses to the atmosphere, and hence arrive at a lower net land flux. We therefore place more trust in the NEP and sum of component values from fire-enabled DGVMs.

The reconciliation between DGVMs and inversions also holds at regional scales. For North America and Russia, both wood harvest and fire disturbance have an important role in regional carbon dynamics (Supplementary Figs. 3 and 4). LULCC gross losses (including peat emissions) are 0.28 ± 0.06 PgC yr^{-1} and 0.19 ± 0.06 PgC yr^{-1}, and fire losses are 0.11 ± 0.02 PgC yr^{-1} and 0.18 ± 0.03 PgC yr^{-1}, respectively. Therefore, net disturbance losses are similar (~0.4 PgC yr^{-1}) in the two regions, however, North America has a larger regrowth sink; 0.5 ± 0.01 PgC yr^{-1}, compared to 0.3 ± 0.1 PgC yr^{-1} for Russia. Combining the disturbance fluxes with the NEP from fire-enabled DGVMs, we estimate net land sinks of 0.9 ± 0.3 PgC
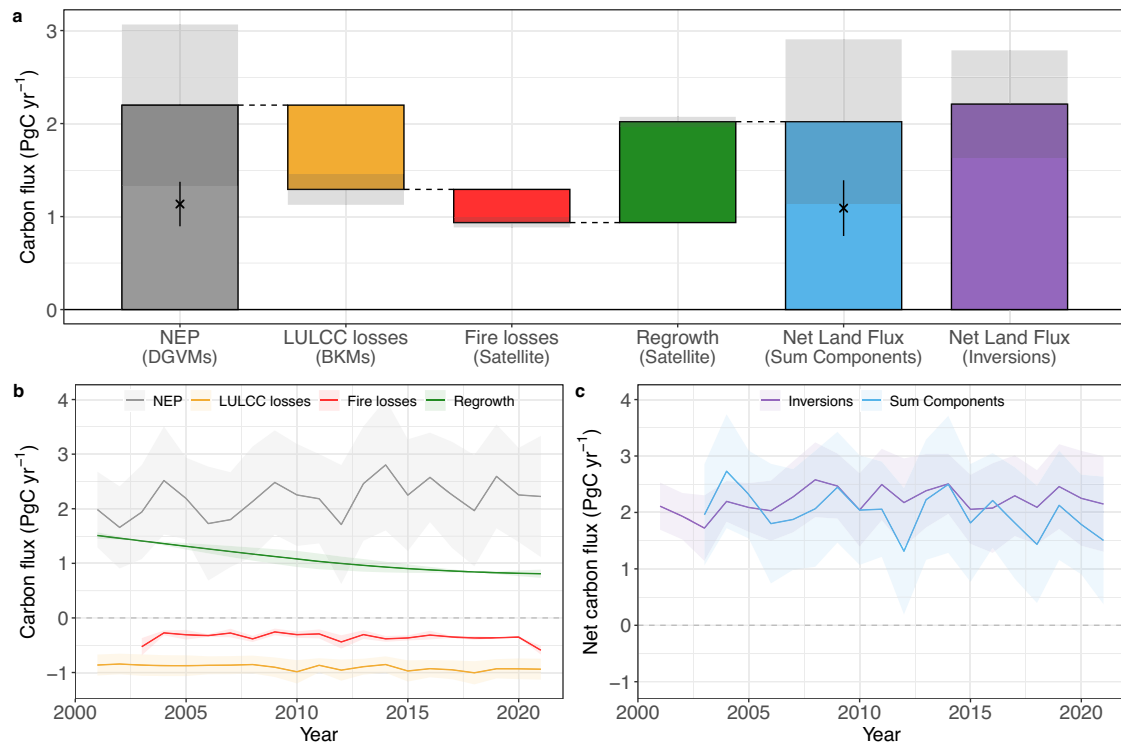
Fig. 4 | Reconciliation and attribution of the northern land carbon sink. a Mean carbon flux over the period 2001–2021 for individual components, for all four regions combined. The carbon sink from rising atmospheric CO_2, nitrogen deposition, and climate change is estimated by the DGVMs (only using fire-enabled DGVMs) from the S2 simulation (grey bar). NEP for non-fire-enabled DGVMs is shown as a cross. Land-use and land cover change gross losses (including peat drainage) are estimated from three bookkeeping models, BLUE, OSCAR, and HN (orange bar). Fire carbon losses are estimated by two satellite-derived products; GFAS and GFED4.1s, for the period 2003–2021 (red bar). The forest regrowth carbon flux is estimated from this study (green). The sum of the four components

(DGVM NEP, Regrowth, LULCC losses, and fire losses) represents our new estimate of the net land sink (light blue bar). The cross on top of the blue bar shows the sum of four components but with NEP from the non-fire enabled models. The net land sink as estimated by atmospheric inversions is also shown (purple). **b, c** Annual mean carbon fluxes for **b** the four component fluxes; NEP (fire-enabled DGVMs only), Regrowth, LULCC losses, and fire losses (positive values mean flux from atmosphere to land), and **c** the sum of the four components (blue), and the net land sink as estimated by the inversions (purple). Shading in all panels represents 1σ uncertainty across the models or inversion datasets, respectively.

yr^{-1}, and 0.6 ± 0.3 PgC yr^{-1}, for North America and Russia. Our estimates agree well with the inversion sinks of 0.8 ± 0.4 PgC yr^{-1} and 0.7 ± 0.3 PgC yr^{-1}, respectively.

For Europe and China, the disturbance-related fluxes are similar. Most disturbance losses are due to wood harvest (total LULCC losses of ~0.2 PgC yr^{-1}), with limited emissions from fire disturbance (<0.04 PgC yr^{-1}, likely due to fire prevention measures, to the exception of extreme fire years in Southern Europe. Both regions have a regrowth flux of 0.2 PgC yr^{-1}, and overall a small net loss of carbon due to disturbance processes. Combining the disturbance fluxes with DGVM NEP leads to bottom-up net land carbon flux estimates of 0.2 ± 0.2 PgC yr^{-1} and 0.3 ± 0.1 PgC yr^{-1}, again in agreement with the inversion estimated sinks of 0.3 ± 0.2 PgC yr^{-1} and 0.4 ± 0.3 PgC yr^{-1}. It is important to note that our analysis does not include carbon losses from all disturbance processes. There are increasing incidences of pest and pathogen outbreaks across northern forests[41–43], which are reducing the land sink. However, wood harvest, deforestation, and fire (which are all included here) together currently still account for the majority of the forest disturbance flux in northern forests[43,44].

Overall, our results indicate it is important to accurately capture disturbance-related losses and gains in order to quantify the magnitude and successfully attribute processes and drivers of the northern carbon sink. In particular, we provide further evidence of the substantial role that age-related disturbance and regrowth has on the contemporary northern carbon sink[11,45–49]. In general, the DGVMs may capture some forest regrowth flux following agricultural abandonment, wood harvest, and fire disturbance. However, this is likely underestimated due to the lack of representation of age classes in most DGVMs, and hence the fast growth of multiple young

trees following disturbance[11,50]. Ecosystem demography is an active area of research and some DGVMs are starting to include the relevant processes to capture age-related dynamics (e.g. refs. 45,51). However, these models are still in the development stage and are not readily available for large-scale simulations. Some models do include demography (CABLE-POP and LPJ-GUESS in this study). CABLE-POP simulates higher carbon uptake in young forests compared to old-growth forests (Supplementary Fig. 5), whereas LPJ-GUESS shows a more even NEP across ages. However, it is not possible to isolate the regrowth flux from other drivers (e.g. CO_2 fertilisation, nitrogen deposition, or changes in climate) with the current modelling protocol. In general, to simulate the large-scale regrowth sink, DGVMs would also need to be informed about the correct disturbance and land management regimes and how they have changed over recent decades, e.g. how forest management has impacted dynamics and stand density, through fire management practices, harvest extraction rates, or historical forest grazing and litter raking[24].

Implications for the global carbon budget
The global net land sink (1.6 ± 0.7 PgC yr^{-1} over 2001–2021) is relatively well constrained by the difference of fossil fuel emissions (9.0 ± 0.5 PgC yr^{-1}) and the sum of the atmospheric growth of CO_2 (4.7 ± 0.02 PgC yr^{-1}) and the global ocean carbon sink (2.6 ± 0.5 PgC yr^{-1}). The DGVMs estimate a similar net global sink of 1.4 ± 0.4 PgC yr^{-1}, but we argue here that this is the right (global) answer for the wrong reasons. In this study, we have provided a bottom-up estimate of the northern land carbon sink that corroborates atmospheric inversion estimates. Further, an alternative set of inversion estimates, that are also constrained with OCO-2 observations of

atmospheric column CO_2, also strongly suggest a northern land carbon sink that is in line with the estimate in this study[29,52]. Therefore, if we accept that the DGVMs underestimate the northern sink, to maintain a global balance, they must overestimate net tropical carbon uptake. DGVMs suggest a net carbon sink of 0.4 ± 0.3 PgC/yr in tropical lands (between 30°S and 30°N), in contrast to the inversions which estimate a carbon loss of 0.1 ± 0.6 PgC/yr[29].

There are a multitude of possibilities for why the DGVMs could overestimate the tropical net carbon sink. Tropical forests are known to be phosphorus limited. As no models used here include this limitation, they could overestimate the CO_2 fertilisation effect in tropical forests[53]. Further, there is growing evidence of increased mortality in tropical forests[54,55], however, DGVMs do not contain drought-mortality formulations[56], simulate the impact of insect outbreaks[56], or consider growth-lifespan tradeoffs[57], and so likely underestimate climate-induced carbon losses. In addition, DGVMs do not fully capture forest degradation processes, which may be as significant as deforestation for total carbon losses[58,59].

In summary, it is highly likely that the global land carbon sink is predominantly located in the young forests of northern regions. The regrowth sink is inherently transient, and so there is potential for the carbon sink to saturate in the future—although a sink can be maintained with sustainable land management practices[60]. Tropical regions could well be a net source of carbon, and tropical carbon losses are likely underestimated by DGVMs. These results could reduce trust we have in current climate projections, as the land carbon sink in Earth System Models (ESMs) is likely overestimated (no age structure or explicit mortality processes). This implies climate-carbon feedbacks are likely underestimated in ESMs, which indicates the remaining carbon budgets (as estimated by ESMs) for a given temperature target are overestimated.

Methods

DGVMs
In this study, we used the net carbon flux from 17 DGVMs that were part of the TRENDY (v11) MIP[1]. The models included are CABLE-POP, CLASSIC, CLM5.0, DLEM, IBIS, ISAM, JSBACHv3.2, JULES-ES, LPJ-GUESS, LPJ, LPX-Bern, OCN, ORCHIDEE, SDGVM, VISIT, VISIT-NIES, and YIBs (see ref. 1 for full model description and setup). The models are driven with a merged monthly Climate Research Unit (CRU)[61] and 6-hourly Japanese 55-year Reanalysis (JRA-55)[62] dataset. The models are also forced with atmospheric CO_2[63], gridded nitrogen deposition[64] and nitrogen fertiliser[65]. CABLE-POP, CLM5.0, DLEM, ISAM, JSBACHv3.2, JULES-ES, LPJ-GUESS, LPX-Bern, OCN, ORCHIDEE, and SDGVM include carbon-nitrogen interactions. CLASSIC, CLM5.0, JSBACH, JULES-ES, LPJ-GUESS, LPJ, LPX-Bern, SDGVM, VISIT, and VISIT-NIES all simulate fire impacts. The net land sink (as shown in Fig. 1) is estimated with the S3 simulation from GCB2022. This includes transient atmospheric CO_2, transient climate, and transient industrial land-use. We use the S2 simulation (transient atmospheric CO_2, transient climate, and fixed pre-industrial land-use) when reconciling the DGVM estimates with inversions as this has no LULCC flux. Note, all acronyms used in this paper are described in the supplementary information (Table S1).

Atmospheric inversions
For the 'top-down' atmospheric constraint on the northern carbon sink, we used eight atmospheric inversion systems from GCB2023 that covered the period 2001–2021; Copernicus Atmosphere Monitoring Service (CAMS v22r1), Jena CarboScope (nbetEXToc_v2023), CarbonTrackerEurope (CTE2023), NISMON-CO2 v2023, CT-NOAA CT2022 + CT-NRT.v2023-3, University of Edinburgh (UoE), IAPCAS, and MIROC (see system description and setups in ref. 29,66). Atmospheric inversion methods estimate ocean and land carbon exchange from atmospheric CO_2 observations. Using Bayesian methods, they optimise carbon fluxes using an atmospheric transport model driven by wind fields from meteorological analyses, prior fluxes and uncertainty fields. The systems impose fossil fuel and cement carbon emissions and small remaining differences between the used emission datasets are adjusted to the common set of GridFED

v2023_1[67] CO_2 emissions (which includes fossil fuel emissions, carbon emissions from cement, and the cement carbonation sink). To allow comparison of these top-down estimates with the DGVMs, a further adjustment for lateral transport of carbon by rivers is needed (see also Section 2.5 in ref. 29). We have applied this lateral adjustment on 1 × 1 degree resolution rather than for the 3 latitude bands as in ref. 29. The lateral river flux is based on GlobalNEWS2 for organic C and the CO_2 sink due to chemical weathering[68,69], with rescaling of the organic C loads to the latitudinal pattern[70] and to a synthesis of global estimates of organic C exports of about 500 Tg C/yr[71].

Wildfire carbon emissions
We use two satellite-derived estimates of wildfire emissions: the Global Fire Emissions Database (GFAS, operated by the Copernicus Atmosphere Monitoring Service[72]) and the Global Fire Emissions Database (GFEDv4.1s[28]). These datasets are two of the most widely applied global fire emissions products based on satellite remote sensing of fire. GFAS relies on the detection of thermal energy release during active fires. GFED relies on the post-fire detection of burned areas combined with fuel consumption factors. As data is only available from 2003 onwards, we use the 2003–2021 mean values for 2001–2002, when calculating means over the whole time period, 2001–2021.

ESA-CCI biomass map
To produce age-dependent regrowth carbon fluxes, we start with a high-resolution (100 m) aboveground biomass product for the year 2010 from the ESA-CCI biomass project (version 4)[26], which is based on remote-sensed synthetic aperture radar, optical, and LiDAR data. We next use the Hansen forest cover mask[73] to isolate forest pixels, and then calculate the mean forest biomass in 1 km grid areas. We convert the original aboveground biomass units of Mg ha^{-1} to MgC ha^{-1} by multiplying by 0.5 (assuming a biomass C content of 50%).

Forest age map
We use the forest age map produced by refs. 25,74 which is representative for the year 2010. This 1 km global map is created by upscaling plot-level forest age data using a random forest model. The forest age data is in part based on the 'GlobBiomass' biomass map[75], along with climate variables as model regressors in the upscaling procedure. To ensure non-forest pixels are excluded, we use the dataset with a 30% tree cover threshold for each 1 km pixel.

Calculating net ecosystem production (NEP)
Eddy-covariance NEP data. We combined multi-years annual NEP data observed from a harmonised dataset of 119 eddy covariance sites in forests where the forest age is known, with age maps from ref. 25 and site specific NEP-age curves from chronosequence locations to scale up regional forest NEP in two steps. The first step is using age. The second step is using the difference between NEP predicted from age only and observed NEP at the 119 locations, and upscaling it using temperature, GPP and age with a random forest model at a spatial resolution of 0.5°. The mean NEP pattern is representative of the last decade. This upscaling accounts for the fact that very young forests are net CO_2 sources to the atmosphere, middle-aged and young forests are sinks and old forests can be small sinks or sources. We call this product EC-Age.

DGVM NEP. The EC-Age data is for forest NEP. We cannot directly estimate forest NEP from DGVMs, as most models have a single soil column for all plant types. Therefore, modelled NEP is calculated as the difference between Net Primary Productivity and Heterotrophic Respiration (NPP-Rh). Here, we add grazing and crop harvest respiration fluxes to Rh. These land management practices are effectively grassland carbon losses in DGVMs, and so simply divert a portion of Rh to separate carbon loss terms. 5 out of 17 models include grazing and/or crop harvest, and so it is important to include these separate loss terms in Rh, to ensure

all 17 DGVMs are aligned. For the reconciliation with inversions (Fig. 4), we use NEP from the S2 simulation, as this does not include LULCC fluxes.

The S2 simulation fixes land cover and land-use at 1700 values, and therefore the NEP fluxes may be biassed. We can quantify this bias by combining the plant-level NEP output from the S2 simulation (transient CO_2, nitrogen deposition, and climate) with present day (we choose 2010 as a reference year) land cover from the S3 simulation. Only one model (ORCHIDEE) has the required detailed output (Supplementary Fig. 6). For North America and China, there has been a net conversion of forest to short vegetation between 1700 and 2010, hence a lower NEP when using 2010 land cover. The opposite is true for Europe and Russia, where there has been a net gain in forest area, and hence NEP, with present land cover, compared to 1700. Overall, however, the differences in regional NEP are relatively small. Our North America and China NEP estimates are overestimated by ~0.02 PgC yr^{-1}, with an underestimation in Europe of ~0.01 PgC yr^{-1}. We make the assumption other models will have a similar bias (same order of magnitude), and therefore this bias does not have a substantial impact on our results.

Estimating regional regrowth

To estimate carbon uptake from forest regrowth over the past two decades, we regressed biomass against forest age. We selected four regions in North America [75°W–95°W, 30°N–36°N], boreal Eurasia [30°E–75°E, 55°N–60°N], temperate Europe [12°W–30°E, 44°N–50°N], and China [106°E–122°E, 24°N–33°N] as training regions. For each age class (we use single years), we calculate the 25th, 50th, and 75th percentiles for all grids that age. We then fit curves to each of the three percentiles, based on Chapman-Richards models[38]. The regrowth curves approach an asymptote, which we defined as the maximum 25th, 50th, 75th percentiles for each age class (single year) across all grids in the region. The best fit model is of the form $B_t = A\left(1 - e^{-kt}\right)^c \pm \varepsilon; A, k, c > 0$, where B_t is the biomass in year t, A is the asymptote, k is the growth rate, and c determines the shape of the curve[76]. We then produce regional tree growth rates by calculating annual differences in the biomass curves. For boreal Eurasia and temperate Europe there is limited data for the youngest forests. We only kept ages with at least 1000 pixel values in our estimation of growth curves. The youngest ages for the two regions in our analysis are therefore 23 and 28 years, respectively. For the relatively few trees younger than this, we assume they have a similar growth rate to these values (Fig. 2e, g). For Norway, Sweden, and Finland, we use the growth rates calculated for boreal Eurasia.

We compare our regrowth rates with those from a meta-analysis of in situ observations[37]. Specifically, we compared the growth rates for North America with North American subtropical humid forest, temperate continental forest, and temperate oceanic forest (mean = 1.4 MgC ha^{-1} yr^{-1}, minimum = 0.6 MgC ha^{-1} yr^{-1}, maximum = 2.7 MgC ha^{-1} yr^{-1}). For boreal Eurasia, we use the Asian boreal coniferous forest (1.1 [0.7,1.4] MgC ha^{-1} yr^{-1}). For Europe, we compare with the European temperate oceanic forest (1.6 [0.8,2.9] MgC ha^{-1} yr^{-1}) data. Finally, for China we use the values specifically for Chinese forests (1.9 [0.6,4.9] MgC ha^{-1}).

For each year in 2001–2021, we calculate the expected biomass increase for each 1 km pixel, depending on the forest age. For the period 2010–2021, we account for disturbances from fire by using the European Space Agency Climate Change Initiative (ESA CCI) burned area product (version 5.1)[27], and reset the age of a pixel to 1 year if any disturbance was detected. In a final step, we multiply each 1 km pixel by the tree cover fraction (ranging from 0 to 1; from ref. 77) to remove non-forest areas (Supplementary Fig. 7). The number of fire disturbed forested pixels in the 2011–2021 period is 3.4%, 1.3%, 6.6%, and 1.3% for North America, Europe, Russia, and China, respectively. The estimated uncertainty in our regrowth estimate stems from the use of quartiles of biomass in the growth curve estimates. The data is approximately distributed equally around the median estimate (Fig. 2), so we convert this IQR range to a standard deviation by multiplying by 1.36 (=68/50) to estimate the ±1σ spread. As a final step, we convert aboveground

to total biomass by using previously published aboveground and belowground carbon densities[78].

LULCC losses

To estimate gross losses from LULCC, we use three bookkeeping models (BKMs) from GCB2023[29]; BLUE, OSCAR, and H&C2023. We exclude any regrowth from the BKMs, to only include gross losses from the land to the atmosphere.

These models simulate carbon stocks in vegetation and soils before and after land-use change events, such as transitions between natural vegetation types, croplands, and pastures. They incorporate literature-based response functions that account for the decay of vegetation and soil carbon, including transfers to product pools with varying lifespans, along with carbon uptake from regrowth processes. Furthermore, the models simulate long-term reductions in carbon stocks of primary forests (by degradation), reflected in lowered carbon levels in both vegetation and soils of secondary forests, and account for forest management activities like wood harvesting.

In addition, we factor in emissions from peatland drainage by using FAO-derived peat drainage emissions[79], emissions from simulations using the DGVM ORCHIDEE-PEAT[80], and estimates from the DGVM LPX-Bern v1.5 model[81].

The three bookkeeping models are driven by different land-use change datasets. H&C2023 derives its estimates from the FAO's Forest Resource Assessment (FRA), which provides forest area and management data at 5-year intervals[82]. Changes in non-forest land uses are derived from FAO's annual national data on cropland and pasture. In contrast, BLUE uses LUH2-GCB2023[29], a harmonized land-use change dataset covering the period 850–2022, with 0.25° spatial resolution, and considers subgrid transitions between different land cover types[83,84]. OSCAR was run with both LUH2-GCB2023 and FAO/FRA data, with the latter extrapolated to 2022 based on trends from 2015–2020. The primary OSCAR estimate in our study is a combination of both data sources.

Data availability

DGVM and BKM output is available at: https://globalcarbonbudgetdata.org/. Atmospheric inversion data is available at: https://meta.icos-cp.eu/objects/FHbD8OTgCb7Tlvs99lUDApO0. Wildfire data is available at: https://ads.atmosphere.copernicus.eu/cdsapp#!/dataset/cams-global-fire-emissions-gfas and https://gwis.jrc.ec.europa.eu/apps/country.profile/downloads. Eddy-covariance NEP data is available at: https://doi.org/10.5281/zenodo.13828536. Regrowth data is available at: https://doi.org/10.5281/zenodo.13844372.

References
1. Friedlingstein, P. et al. Global carbon budget 2022. *Earth Syst. Sci. Data* **14**, 4811–4900 (2022).
2. Ciais, P. et al. Five decades of northern land carbon uptake revealed by the interhemispheric CO_2 gradient. *Nature* **568**, 221–225 (2019).
3. Gaubert, B. et al. Global atmospheric CO_2 inverse models converging on neutral tropical land exchange, but disagreeing on fossil fuel and atmospheric growth rate. *Biogeosciences* **16**, 117–134 (2019).
4. Bastos, A. et al. Sources of uncertainty in regional and global terrestrial CO_2 exchange estimates. *Glob. Biogeochem. Cycles* **34**, e2019GB006393 (2020).
5. Forkel, M. et al. Enhanced seasonal CO_2 exchange caused by amplified plant productivity in northern ecosystems. *Science* **351**, 696–699 (2016).
6. Nemani, R. R. et al. Climate-driven increases in global terrestrial net primary production from 1982 to 1999. *Science* **300**, 1560–1563 (2003).

7. O'Sullivan, M. et al. Have synergies between nitrogen deposition and atmospheric CO_2 driven the recent enhancement of the terrestrial carbon sink? *Glob. Biogeochem. Cycles* **33**, 163–180 (2019).

8. Zaehle, S. & Friend, A. D. Carbon and nitrogen cycle dynamics in the O-CN land surface model: 1. Model description, site-scale evaluation, and sensitivity to parameter estimates. *Glob. Biogeochem. Cycles* **24**, 1–13 (2010).

9. Walker, A. P. et al. Decadal biomass increment in early secondary succession woody ecosystems is increased by CO_2 enrichment. *Nat. Commun.* **10**, 454 (2019).

10. Schimel, D., Stephens, B. B. & Fisher, J. B. Effect of increasing CO_2 on the terrestrial carbon cycle. *Proc. Natl Acad. Sci. USA* **112**, 436–441 (2015).

11. Pugh, T. A. M. et al. Role of forest regrowth in global carbon sink dynamics. *Proc. Natl Acad. Sci. USA* **116**, 4382–4387 (2019).

12. O'Sullivan, M. et al. Process-oriented analysis of dominant sources of uncertainty in the land carbon sink. *Nat. Commun.* **13**, 4781 (2022).

13. Canadell, J. G., Monteiro, P. M. S., Costa, M. H. & Da Cunha, L. C. Global carbon and other biogeochemical cycles and feedbacks. in *Climate Change 2021 – The Physical Science Basis: Working Group I Contribution to the Sixth Assessment Report of the Intergovernmental Panel on Climate Change* (2021).

14. Tagesson, T. et al. Recent divergence in the contributions of tropical and boreal forests to the terrestrial carbon sink. *Nat. Ecol. Evol.* **4**, 202–209 (2020).

15. Kondo, M. et al. Plant regrowth as a driver of recent enhancement of terrestrial CO_2 uptake. *Geophys. Res. Lett.* **45**, 4820–4830 (2018).

16. Houghton, R. A. & Nassikas, A. A. Global and regional fluxes of carbon from land use and land cover change 1850–2015. *Global Biogeochem. Cycles* **31**, 456–472 (2017).

17. Li, F. et al. Historical (1700–2012) global multi-model estimates of the fire emissions from the Fire Modeling Intercomparison Project (FireMIP). *Atmos. Chem. Phys.* **19**, 12545–12567 (2019).

18. Arneth, A. et al. Historical carbon dioxide emissions caused by land-use changes are possibly larger than assumed. *Nat. Geosci.* **10**, 79–84 (2017).

19. Williams, C. A., Collatz, G. J. & Masek, J. Carbon consequences of forest disturbance and recovery across the conterminous United States. *Global Biogeochem. Cycles* https://doi.org/10.1029/2010GB003947 (2012).

20. Goetz, S. J. et al. Observations and assessment of forest carbon dynamics following disturbance in North America. *JGR Biogeosci.* **117**, 1–17 (2012).

21. Fu, Z. et al. Recovery time and state change of terrestrial carbon cycle after disturbance. *Environ. Res. Lett.* **12**, 104004 (2017).

22. Lindeskog, M. et al. Accounting for forest management in the estimation of forest carbon balance using the dynamic vegetation model LPJ-GUESS (v4.0, r9710): implementation and evaluation of simulations for Europe. *Geosci. Model Dev.* https://doi.org/10.5194/gmd-14-6071-2021 (2021).

23. Pugh, T. A. M. et al. Simulated carbon emissions from land-use change are substantially enhanced by accounting for agricultural management. *Environ. Res. Lett.* **10**, 124008 (2015).

24. Erb, K.-H. et al. Bias in the attribution of forest carbon sinks. *Nat. Clim. Chang.* **3**, 854–856 (2013).

25. Besnard, S. et al. Mapping global forest age from forest inventories, biomass and climate data. *Earth Syst. Sci. Data* **13**, 4881–4896 (2021).

26. Santoro, M. & Cartus, O. ESA Biomass Climate Change Initiative (Biomass_cci): Global datasets of forest above-ground biomass for the years 2010, 2017, 2018, 2019 and 2020, v4 (NERC EDS Centre for Environmental Data Analysis, 2023).

27. Chuvieco, E., Pettinari, M. L., Lizundia-Loiola, J., Storm, T. & Padilla Parellada, M. ESA fire climate change initiative (fire_cci): MODIS fire_cci burned area pixel product, version 5.1. https://doi.org/10.

5285/58F00D8814064B79A0C49662AD3AF537 (Centre for Environmental Data Analysis (CEDA), 2018).

28. van der Werf, G. R. et al. Global fire emissions estimates during 1997–2016. *Earth Syst. Sci. Data* **9**, 697–720 (2017).

29. Friedlingstein, P. et al. Global carbon budget 2023. *Earth Syst. Sci. Data* **15**, 5301–5369 (2023).

30. Vallet, L. et al. Soil smoldering in temperate forests: a neglected contributor to fire carbon emissions revealed by atmospheric mixing ratios. *EGUsphere* https://doi.org/10.5194/egusphere-2023-2421 (2023).

31. Shvidenko, A. Z. et al. Impact of wildfire in Russia between 1998–2010 on ecosystems and the global carbon budget. *Dokl. Earth Sci.* **441**, 1678–1682 (2011).

32. Zheng, B. et al. Record-high CO_2 emissions from boreal fires in 2021. *Science* **379**, 912–917 (2023).

33. West, P. W. Do increasing respiratory costs explain the decline with age of forest growth rate? *J. Forestry Res.* **31**, 693–712 (2020).

34. Coomes, D. A., Holdaway, R. J., Kobe, R. K., Lines, E. R. & Allen, R. B. A general integrative framework for modelling woody biomass production and carbon sequestration rates in forests. *J. Ecol.* **100**, 42–64 (2012).

35. Fan, L. et al. Siberian carbon sink reduced by forest disturbances. *Nat. Geosci.* **16**, 56–62 (2022).

36. O'Sullivan, M. et al. Climate-driven variability and trends in plant productivity over recent decades based on three global products. *Glob. Biogeochem. Cycles* **34**, e2020GB006613 (2020).

37. Cook-Patton, S. C. et al. Mapping carbon accumulation potential from global natural forest regrowth. *Nature* **585**, 545–550 (2020).

38. Richards, F. J. A flexible growth function for empirical use. *J. Exp. Bot.* **10**, 290–301 (1959).

39. Friedl, M. A. et al. A tale of two springs: using recent climate anomalies to characterize the sensitivity of temperate forest phenology to climate change. *Environ. Res. Lett.* **9**, 054006 (2014).

40. Keenan, T. F. et al. Net carbon uptake has increased through warming-induced changes in temperate forest phenology. *Nat. Clim. Chang.* **4**, 598–604 (2014).

41. Patacca, M. et al. Significant increase in natural disturbance impacts on European forests since 1950. *Glob. Chang. Biol.* **29**, 1359–1376 (2023).

42. Korosuo, A. et al. The role of forests in the EU climate policy: are we on the right track? *Carbon Balance Manag.* **18**, 15 (2023).

43. Fei, S., Morin, R. S., Oswalt, C. M. & Liebhold, A. M. Biomass losses resulting from insect and disease invasions in US forests. *Proc. Natl Acad. Sci. USA* **116**, 17371–17376 (2019).

44. Harris, N. L. et al. Attribution of net carbon change by disturbance type across forest lands of the conterminous United States. *Carbon Balance Manag.* **11**, 24 (2016).

45. Zaehle, S. et al. The importance of age-related decline in forest NPP for modeling regional carbon balances. *Ecol. Appl.* **16**, 1555–1574 (2006).

46. Luyssaert, S. et al. The European carbon balance. Part 3: forests. *Glob. Chang. Biol.* **16**, 1429–1450 (2010).

47. Kohlmaier, G. H. et al. Effects of the age class distributions of the temperate and boreal forests on the global CO_2 source-sink function. *Tellus B Chem. Phys. Meteorol.* **47**, 212–231 (1995).

48. Winkler, K. et al. Changes in land use and management led to a decline in Eastern Europe's terrestrial carbon sink. *Commun. Earth Environ.* **4**, 1–14 (2023).

49. Yang, H. et al. Global increase in biomass carbon stock dominated by growth of northern young forests over past decade. *Nat. Geosci.* **16**, 886–892 (2023).

50. Burton, C. et al. Representation of fire, land-use change and vegetation dynamics in the Joint UK Land Environment Simulator vn4.9 (JULES). *Geosci. Model Dev.* **12**, 179–193 (2019).

51. Argles, A. P. K. et al. Robust Ecosystem Demography (RED version 1.0): a parsimonious approach to modelling vegetation dynamics in Earth system models. *Geosci. Model Dev.* **13**, 4067–4089 (2020).

52. Byrne, B. et al. National CO_2 budgets (2015–2020) inferred from atmospheric CO_2 observations in support of the global stocktake. *Earth Syst. Sci. Data* **15**, 963–1004 (2023).

53. Cunha, H. F. V. et al. Direct evidence for phosphorus limitation on Amazon forest productivity. *Nature* **608**, 558–562 (2022).

54. Hubau, W. et al. Asynchronous carbon sink saturation in African and Amazonian tropical forests. *Nature* **579**, 80–87 (2020).

55. Brienen, R. J. W. et al. Long-term decline of the Amazon carbon sink. *Nature* **519**, 344–348 (2015).

56. McDowell, N. et al. Drivers and mechanisms of tree mortality in moist tropical forests. *N. Phytol.* **219**, 851–869 (2018).

57. Brienen, R. J. W. et al. Forest carbon sink neutralized by pervasive growth-lifespan trade-offs. *Nat. Commun.* **11**, 4241 (2020).

58. Matricardi, E. A. T. et al. Long-term forest degradation surpasses deforestation in the Brazilian Amazon. *Science* **369**, 1378–1382 (2020).

59. Lapola, D. M. et al. The drivers and impacts of Amazon forest degradation. *Science* **379**, eabp8622 (2023).

60. Ontl, T. A. et al. Forest management for carbon sequestration and climate adaptation. *J. Forestry* **118**, 86–101 (2019).

61. Harris, I., Osborn, T. J., Jones, P. & Lister, D. Version 4 of the CRU TS monthly high-resolution gridded multivariate climate dataset. *Sci. Data* **7**, 109 (2020).

62. Kobayashi, S. et al. The JRA-55 reanalysis: general specifications and basic characteristics. 気象集誌. 第2輯 **93**, 5–48 (2015).

63. Dlugokencky, E. & Tans, P. Trends in atmospheric carbon dioxide. National Oceanic and Atmospheric Administration, EarthSystem Research Laboratory (NOAA/ESRL). http://www.esrl.noaa.gov/gmd/ccgg/trends/global.html (2022).

64. Hegglin, M., Kinnison, D. & Lamarque, J.-F. CCMI nitrogen surface fluxes in support of CMIP6 - version 2.0. https://doi.org/10.22033/ESGF/INPUT4MIPS.1125 (Earth System Grid Federation, 2016).

65. Lu, C. & Tian, H. Global nitrogen and phosphorus fertilizer use for agriculture production in the past half century: shifted hot spots and nutrient imbalance. *Earth Syst. Sci. Data* **9**, 181–192 (2017).

66. Luijkx, I. T. et al. *Global CO_2 Gridded Flux Fields from 14 Atmospheric Inversions in GCB2023*. https://doi.org/10.18160/4M52-VCRU (ICOS Carbon Portal, 2024).

67. Jones, M. W. et al. *Gridded Fossil CO_2 Emissions and Related O_2 Combustion Consistent with National Inventories*. https://doi.org/10.5281/zenodo.8386803 (2023).

68. Zscheischler, J. et al. Reviews and syntheses: an empirical spatiotemporal description of the global surface–atmosphere carbon fluxes: opportunities and data limitations. *Biogeosciences* **14**, 3685–3703 (2017).

69. Hartmann, J., Jansen, N., Dürr, H. H., Kempe, S. & Köhler, P. Global CO2-consumption by chemical weathering: what is the contribution of highly active weathering regions? *Glob. Planet. Change* **69**, 185–194 (2009).

70. Resplandy, L. et al. Revision of global carbon fluxes based on a reassessment of oceanic and riverine carbon transport. *Nat. Geosci.* **11**, 504–509 (2018).

71. Regnier, P. et al. Anthropogenic perturbation of the carbon fluxes from land to ocean. *Nat. Geosci.* **6**, 597–607 (2013).

72. Di Giuseppe, F., Rémy, S., Pappenberger, F. & Wetterhall, F. Using the Fire Weather Index (FWI) to improve the estimation of fire emissions from fire radiative power (FRP) observations. *Atmos. Chem. Phys.* **18**, 5359–5370 (2018).

73. Hansen, M. C. et al. High-resolution global maps of 21st-century forest cover change. *Science* **342**, 850–853 (2013).

74. Besnard, S. et al. Quantifying the effect of forest age in annual net forest carbon balance. *Environ. Res. Lett.* **13**, 124018 (2018).

75. Santoro, M. *GlobBiomass—Global Datasets of Forest Biomass*. https://doi.org/10.1594/PANGAEA.894711 (PANGAEA, 2018).

76. Heinrich, V. H. A. et al. Large carbon sink potential of secondary forests in the Brazilian Amazon to mitigate climate change. *Nat. Commun.* **12**, 1785 (2021).

77. Tuanmu, M.-N. & Jetz, W. A global 1-km consensus land-cover product for biodiversity and ecosystem modelling. *Glob. Ecol. Biogeogr.* **23**, 1031–1045 (2014).

78. Spawn, S. A., Sullivan, C. C., Lark, T. J. & Gibbs, H. K. Harmonized global maps of above and belowground biomass carbon density in the year 2010. *Sci. Data* **7**, 112 (2020).

79. Conchedda, G. & Tubiello, F. N. Drainage of organic soils and GHG emissions: validation with country data. *Earth Syst. Sci. Data* **12**, 3113–3137 (2020).

80. Qiu, C. et al. Large historical carbon emissions from cultivated northern peatlands. *Sci. Adv.* **7**, 1–10 (2021).

81. Müller, J. & Joos, F. Committed and projected future changes in global peatlands—continued transient model simulations since the Last Glacial Maximum. *Biogeosciences* **18**, 3657–3687 (2021).

82. Food and Agriculture Organization. *Global Forest Resources Assessment 2020: Main Report* (Food & Agriculture Organization of the United Nations (FAO), 2020).

83. Hurtt, G. C. et al. Harmonization of global land use change and management for the period 850–2100 (LUH2) for CMIP6. *Geosci. Model Dev.* **13**, 5425–5464 (2020).

84. Chini, L. et al. Land-use harmonization datasets for annual global carbon budgets. *Earth Syst. Sci. Data* **13**, 4175–4189 (2021).

Acknowledgement

Author contributions

M.O.S. designed the concept and methodological process of the study with input from S.S. and P.F. M.O.S. carried out main data analysis with support from T.M.R. M.O.S. wrote the initial draft of the manuscript. P.C. provided the EC-Age dataset. J.P., C.S., T.G. and R.H. provided the bookkeeping model data. All authors provided feedback on methodology, manuscript and interpretation of results. I.T.L., W.P., N.C., F.C., L.F., Y.N., P.I.P., P.P., C.R. and D.Y. provided the inversion results. A.A., V.K.A., S.F., A.K.J., E.K., D.K., J.K., M.J.M., M.O.S., B.P., Q.S., H.T., A.P.W., W.Y., X.Y. and S.Z. provided DGVM results.

Competing interests

Prabir Patra is an Editorial Board Member for *Communications Earth & Environment*, but was not involved in the editorial review of, nor the decision to publish this article. All other authors declare no competing interests.

Additional information

Supplementary information The online version contains supplementary material available at https://doi.org/10.1038/s43247-024-01827-4.

Correspondence and requests for materials should be addressed to Michael O'Sullivan.

Peer review information *Communications Earth & Environment* thanks the anonymous reviewers for their contribution to the peer review of this work. Primary Handling Editor: Joe Aslin. A peer review file is available.

Reprints and permissions information is available at http://www.nature.com/reprints

Publisher's note Springer Nature remains neutral with regard to jurisdictional claims in published maps and institutional affiliations.

[1]Faculty of Environment, Science and Economy, University of Exeter, Exeter EX4 4QF, UK. [2]Laboratoire de Météorologie Dynamique/Institut Pierre-Simon Laplace, CNRS, Ecole Normale Supérieure/Université PSL, Sorbonne Université, Ecole Polytechnique, Paris, France. [3]Environmental Sciences Group, Wageningen University, P.O. Box 47, 6700AA Wageningen, The Netherlands. [4]Karlsruhe Institute of Technology, Institute of Meteorology and Climate Research/Atmospheric Environmental Research, 82467 Garmisch-Partenkirchen, Germany. [5]Canadian Centre for Climate Modelling and Analysis, Victoria, BC, Canada. [6]Research Institute for Global Change, JAMSTEC, Yokohama 236 001, Japan. [7]Laboratoire des Sciences du Climat et de l'Environnement, LSCE/IPSL, CEA-CNRS-UVSQ, Université Paris-Saclay, F-91198 Gif-sur-Yvette, France. [8]Ludwig-Maximilians-Universität München, Luisenstr. 37, 80333 München, Germany. [9]National Centre for Earth Observation, University of Edinburgh, Edinburgh EH9 3FE, UK. [10]School of Geosciences, University of Edinburgh, Edinburgh, UK. [11]International Institute for Applied Systems Analysis (IIASA), Schlossplatz 1, A-2361 Laxenburg, Austria. [12]Woodwell Climate Research Center, Falmouth, MA 02540, USA. [13]Department of Atmospheric Sciences, University of Illinois, Urbana, IL 61821, USA. [14]Institute of Applied Energy (IAE), Minato-ku, Tokyo 105-0003, Japan. [15]National Center for Atmospheric Research, Climate and Global Dynamics, Terrestrial Sciences Section, Boulder, CO 80305, USA. [16]Hawkesbury Institute for the Environment, Western Sydney University, Penrith, NSW, Australia. [17]CSIRO Environment, Canberra, ACT 2101, Australia. [18]Earth System Division, National Institute for Environmental Studies, 16-2 Onogawa, Tsukuba, Ibaraki 305-8506, Japan. [19]Department of Climate and Geochemistry Research, Meteorological Research Institute, 1-1 Nagamine, Tsukuba, Ibaraki 305-0052, Japan. [20]Research Institute for Humanity and Nature, Kyoto 603 8047, Japan. [21]Max Planck Institute for Meteorology, Bundesstraße 53, 20146 Hamburg, Germany. [22]Biospheric Sciences Laboratory, NASA Goddard Space Flight Center, Greenbelt, MD 20771, USA. [23]Max Planck Institute for Biogeochemistry, P.O. Box 600164 Hans-Knöll-Str. 10, 07745 Jena, Germany. [24]Climate and Environmental Physics, Physics Institute, University of Bern, Bern, Switzerland. [25]Oeschger Centre for Climate Change Research, University of Bern, Bern, Switzerland. [26]Schiller Institute for Integrated Science and Society, Department of Earth and Environmental Sciences, Boston College, Chestnut Hill, MA 02467, USA. [27]Environmental Sciences Division and Climate Change Science Institute, Oak Ridge National Laboratory, Oak Ridge, TN 37831, USA. [28]Carbon Neutrality Research Center, Institute of Atmospheric Physics, Chinese Academy of Sciences, Beijing 100029, China. [29]School of Atmospheric Sciences, Sun Yat-sen University, Zhuhai, Guangdong 510245, China. [30]School of Environmental Science and Engineering, Nanjing University of Information Science and Technology (NUIST), Nanjing, China. ✉e-mail: m.osullivan@exeter.ac.uk